# Hydrogen-Catalyzed, Pilot-Scale Production of Small-Diameter Boron Nitride Nanotubes and Their Macroscopic Assemblies

Keun Su Kim, Christopher T. Kingston, Amy Hrdina, Michael B. Jakubinek, Jingwen Guan, Mark Plunkett, and Benoit Simard*

Security and Disruptive Technologies Portfolio, Emerging Technologies Division, National Research Council Canada, Ottawa, ON K1A 0R6, Canada

ABSTRACT Boron nitride nanotubes (BNNTs) exhibit a range of properties that are as compelling as those of carbon nanotubes (CNTs); however, very low production volumes have prevented the science and technology of BNNTs from evolving at even a fraction of the pace of CNTs. Here we report the high-yield production of small-diameter BNNTs from pure hexagonal boron nitride powder in an induction thermal plasma process. Few-walled, highly crystalline

small-diameter BNNTs ($\sim$5 nm) are produced exclusively and at an unprecedentedly high rate approaching 20 g/h, without the need for metal catalysts. An exceptionally high cooling rate ($\sim 10^5$ K/s) in the induction plasma provides a strong driving force for the abundant nucleation of small-sized B droplets, which are known as effective precursors for small-diameter BNNTs. It is also found that the addition of hydrogen to the reactant gases is crucial for achieving such high-quality, high-yield growth of BNNTs. In the plasma process, hydrogen inhibits the formation of N_2 from N radicals and promotes the creation of B$-$N$-$H intermediate species, which provide faster chemical pathways to the re-formation of a h-BN-like phase in comparison to nitridation from N_2. We also demonstrate the fabrication of macroscopic BNNT assemblies such as yarns, sheets, buckypapers, and transparent thin films at large scales. These findings represent a seminal milestone toward the exploitation of BNNTs in real-world applications.
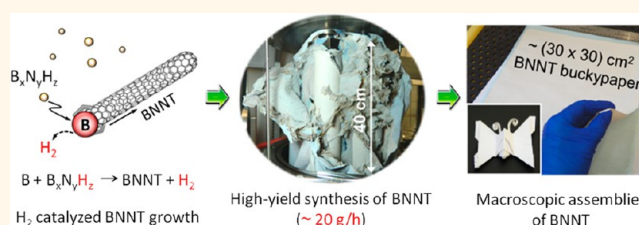
KEYWORDS: boron nitride nanotubes · large scale · high-quality small diameter · induction thermal plasma · macroscopic assemblies

Boron nitride nanotubes (BNNTs) have the same tubular structures and geometries as carbon nanotubes (CNTs) on the molecular scale, resulting in similar exceptional mechanical properties to their carbon counterparts.[1] Unlike CNTs, BNNTs have a much wider band gap ($\sim$5.5 eV),[2] partially ionic structure,[3] and greater thermal stability,[4] making them appealing for use in both mechanical reinforcement applications in which CNTs might be used and also in transparent bulk composites, high-temperature materials, and radiation shielding, for which CNTs are not well-suited. Despite having been first synthesized in 1995,[5] large-scale production of BNNTs remains a significant challenge, which is a clear bottleneck in developing the science and technologies to exploit them.

Several processes have been explored for large-scale synthesis of BNNTs,[6–9] such as arc discharge,[10] laser ablation,[11] chemical vapor deposition,[12–14] ball milling—annealing,[15,16] pyrolysis,[17] and arc-jet plasma.[18] Most are fundamentally similar to those used to produce CNTs but with synthesis conditions that often differ substantially from those optimized for CNT growth. The larger-scale production methods have demonstrated that pure and highly crystalline BNNTs can be produced at relatively high-yield rates of $\sim$1 g/h;[8,19] however, BNNTs synthesized via those routes usually have relatively large diameters (>50 nm), frequently with segmented herringbone or bamboo structures.[15,16] To fully take advantage of the distinct phenomena occurring at nanoscales, highly crystalline small-diameter BNNTs are more favorable.

Only a few methods have been demonstrated to be suitable for the synthesis of small-diameter (<10 nm), highly crystalline BNNTs.[20–25] Yu et al. reported that smaller

BNNTs can be produced in a ball milling−annealing process by changing the reaction gas from N_2 to NH_3.[22] In this work, several grams of amorphous boron powder were loaded in the milling jar, subjected to 150 h of ball milling, followed by 16 h of annealing. By employing Li_2O as a precursor in the boron oxide (BO) CVD method, Huang *et al.* reported reduction of BNNT diameter below 10 nm and demonstrated production of 50 mg of BNNT sample in 3 h (*i.e.*, 0.016 g/h).[25] Smith *et al.* also reported production of 60 mg of ultrafine BNNT sample in 30 min (*i.e.*, 0.12 g/h) *via* the pressurized vapor/condenser method.[24] However, these processes have still been limited to yields on the order of tens of milligrams per hour (<0.2 g/h), or below, meaning that availability of multigram quantities of high-quality small-diameter BNNTs for applications development remains a significant challenge.

Here we report a new industrially scalable plasma process for the continuous production of highly crystalline, small-diameter (∼5 nm) BNNTs at a rate approaching 20 g/h with demonstrated single-experiment synthesis close to 200 g. In this work, BNNTs are synthesized continuously from an induction thermal plasma reactor (Supporting Information Figure S1) that is similar to one previously reported for the production of single-walled carbon nanotubes.[26] It is found that the unique thermal flow inside the reactor (*i.e.*, high cooling rate of ∼10^5 K/s) enhances the formation of small-diameter B droplets exclusively, which are effective precursors for small-diameter BNNTs. We also found that the presence of hydrogen in the reactant gases is crucial for achieving such high-quality, high-yield growth of BNNTs from B droplets. This catalytic effect of hydrogen is striking as such an effect has not previously been reported for BNNT synthesis. The critical role of hydrogen in the high-yield growth of BNNTs is discussed in connection with the nitridation efficiency of B droplets during the process. In addition, we make the first demonstrations of the production of macroscopic yarns, sheets, buckypapers, and transparent thin films of BNNTs at large scales, which are important first steps toward the development of applications.

RESULTS AND DISCUSSION

High-Yield Synthesis of BNNTs. In a typical synthesis experiment, solid hexagonal boron nitride (h-BN) powder was fed along with nitrogen and hydrogen gases into the high-temperature plasma (>8000 K, Figure S2) at atmospheric pressure. Boron powder was also explored as a starting material; however, this approach was found to be very inefficient, resulting in a highly B-rich powder. This result is discussed further in Supporting Information. In all experiments, no metallic catalyst was added. The feedstock materials were vaporized immediately (∼ms) inside the plasma, decomposing into the constituent elements (B, N, and H). The exceptionally high cooling rate within the reactor

(∼10^5 K/s, Figure S2) promoted the subsequent formation of nanosized boron droplets from which BNNTs grew rapidly to a few micrometers in length by the incorporation of nitrogen-containing species from the reaction stream (*i.e.*, root growth mechanism, Figure S3).[27] This renitridation of B following feedstock vaporization is a crucial factor in achieving high-yield conversion of h-BN into BNNTs. More details on the nucleation and growth mechanism of BNNTs in our process are discussed in the next section.

The presence of hydrogen in the reactant gases was found to be essential to the production of BNNTs. In the absence of hydrogen, similar to previous work,[18] the product contains large amounts of amorphous boron powder with very few, if any, BNNTs (Figure S4). However, we observed that substantial quantities of BNNTs, with an unprecedentedly high-yield rate approaching 20 g/h, could be realized by incorporating a well-controlled quantity of hydrogen in the plasma gas and that the rate of recovery of material in our process was very sensitive to the partial pressure of hydrogen. For instance, by increasing hydrogen from 13 to 18 vol %, the recovery rate was improved by a factor of 1.3. The effect of hydrogen in this process is striking as the necessity of hydrogen in the high-yield growth of BNNTs has not been demonstrated in prior literature. Previous reports[22,28] have shown that the use of hydrogen-containing gases (*e.g.*, NH_3) during synthesis could influence the diameter distribution of the BNNTs, but no significant influence on yield was reported. In this work, we did not observe any impact on diameter distribution with varying hydrogen content.

Figure 1 shows photographs of the reaction products collected following an 11 h synthesis experiment. The slight beige coloring of the material is due to light contamination by amorphous boron, a byproduct of the process due to the tendency for N atoms liberated from h-BN during vaporization to recombine as N_2 (discussed in greater detail below). The amorphous boron is easily removable through a thermal oxidation treatment, yielding a snow-white material (Figure S10). In this experiment, 192 g of material was produced. The production rate approaches 20 g/h, which is >100 times higher than what has been reported in the literature to date for structurally similar BNNTs[24,25] or close to 20 times the rates reported for larger-diameter BNNTs.[8,19] Figure 1 also shows that the as-grown BNNT material exhibits three distinct morphologies depending on where and how it deposits within the reactor, which is another unique characteristic of this plasma process. Entangled fibrils (Figure 1C), macroscopic cloth-like sheets (Figure 1D), and very low density cotton-like deposits (Figure 1E) are formed as a result of gas-flow-driven segregation of BNNT materials in the course of the collection. The structural quality of the BNNT is the same within these different materials; only the macroscopic morphologies differ.
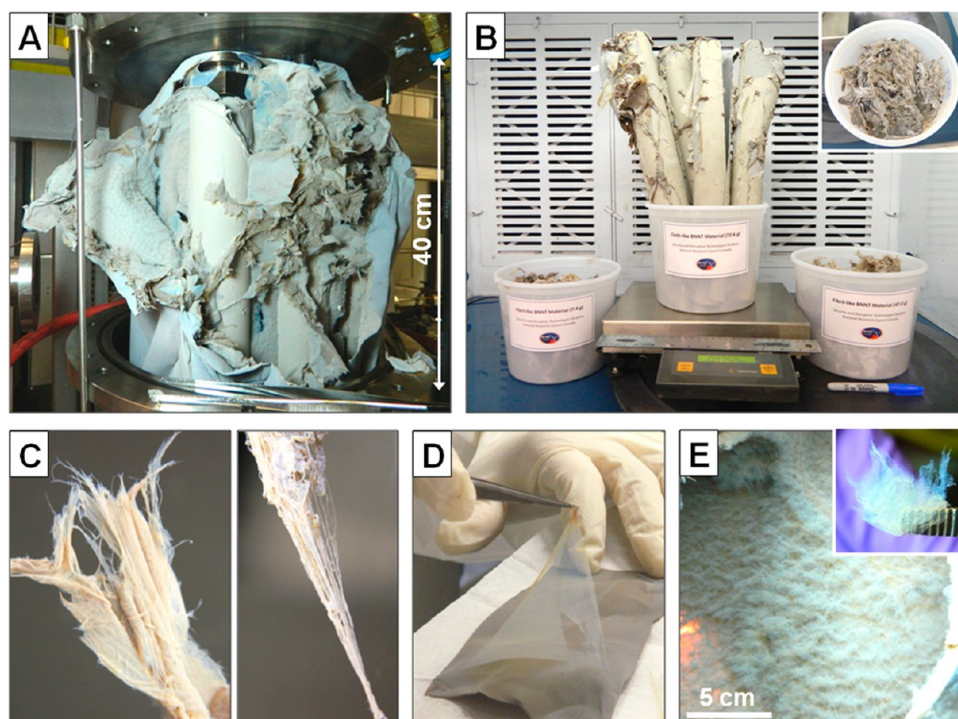
Figure 1. Photos of the BNNT materials grown by an induction plasma process. (A) Reaction product in the filtration chamber following an 11 h synthesis experiment. (B) BNNT materials collected from the filtration chamber. In total, 192 g of BNNT material was synthesized in a single experiment, demonstrating a high-yield rate approaching 20 g/h. The as-grown BNNT materials also exhibit three distinct morphologies of entangled fibrils, cloth-like sheets, and fluffy cotton-like deposits. (C) Fibril materials consist of many fibrils formed naturally, and BNNT yarns can be drawn directly from them. (D) Cloth-like sheets have a multilayered structure, and thin diaphanous membranes are easily peeled off. (E) Fluffy cotton-like deposits have a low density and cover the entire wall of the filtration chamber. Inset is a close-up image.
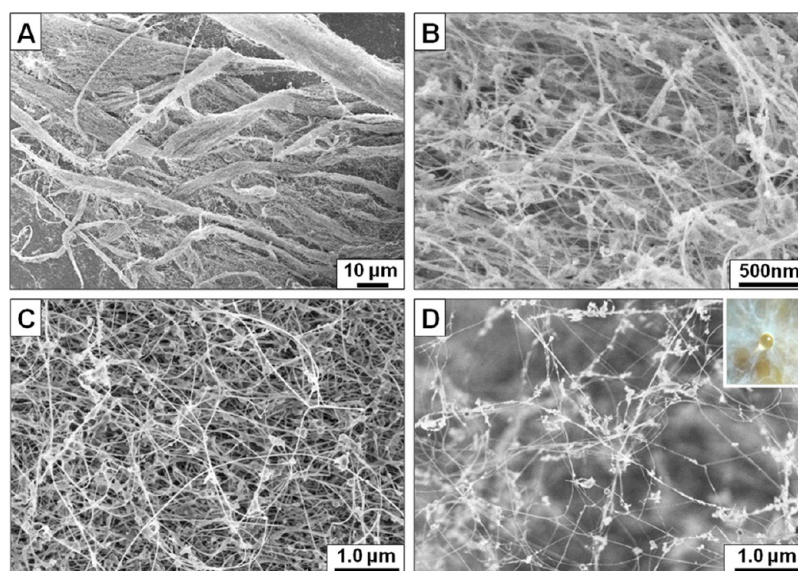

Figure 2. SEM images of the as-grown BNNT materials with three different morphologies. (A) Low-magnification image of the fibril material shows many micrometer-sized strands aligned in a common direction. (B) Its high-magnification image reveals that the strands are composed of densely packed aligned BNNTs. (C) Image of the cloth-like sheet. Randomly entangled BNNTs are observed. (D) Image of the fluffy cotton-like deposit. Unlike the other two material morphologies, the density of BNNTs in this sample is very low, which contributes to interesting physicochemical properties, such as superhydrophobicity (inset) and a strong photoacoustic effect (Supporting Information video S1).

Figure 2 presents SEM images of as-grown BNNT materials at different magnifications. The fibril material consists of numerous fibrous strands formed naturally during the synthesis process. At lower magnification (Figure 2A), it is observed that these fibrils are composed of many micrometer-sized strands that are
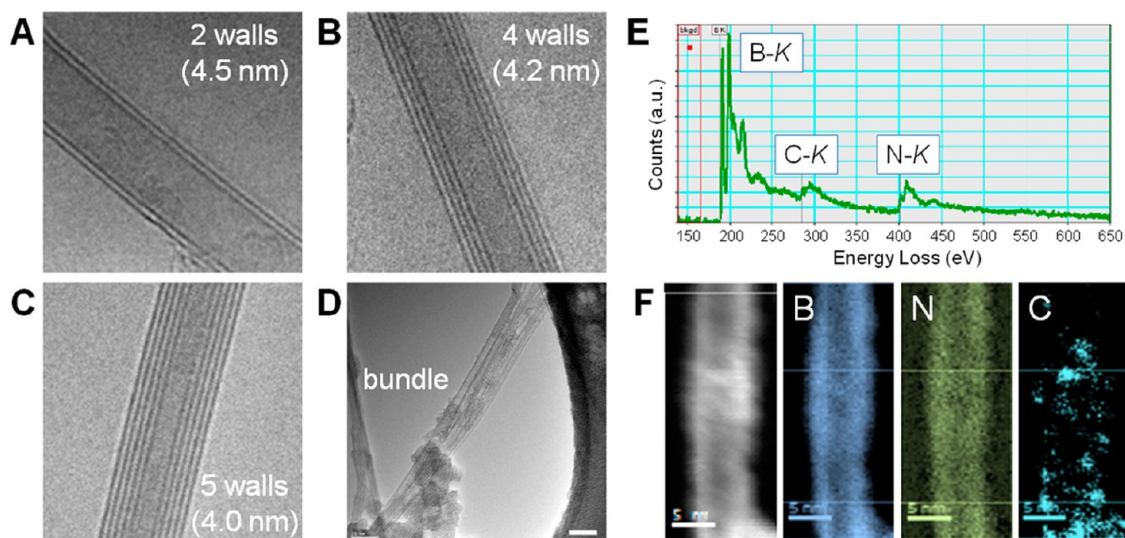
Figure 3. TEM analysis on the as-grown BNNT materials. TEM images of a two-walled BNNT (A), a four-walled BNNT (B), and a five-walled BNNT (C). The walls of the BNNT are defect-free, demonstrating their high structural quality. (D) TEM image of a small BNNT bundle. The scale bar is 20 nm. (E) EELS spectrum of a BNNT with a diameter of ~5 nm. The K-shell ionization edges of B (189 eV) and N (401 eV) are observed and confirm the presence of B and N in the nanotube. (F) Zero-loss energy-filtered image of the nanotube and its elemental maps. The elemental maps of B and N clearly reveal that B and N are the constituent species of the nanotube, whereas the C map indicates carbon contamination on the outer surface of the nanotube.

coalesced with coarse alignment along the fibril axis. Higher magnification imaging (Figure 2B) shows that each strand consists of densely packed BNNTs with a similar degree of alignment along the strand axis. These BNNTs were synthesized in free space, without substrates, and were found to be bridging open gaps between the walls and filter elements (Figure S1) of the reactor, meaning that the observed alignment is entirely a self-assembly process. Images of the cloth-like (Figure 2C) and low-density (Figure 2D) deposits show randomly oriented BNNTs along with nontubular materials that have been identified as primarily few-layered h-BN fragments, either from incompletely vaporized feedstock or byproducts of the BNNT synthesis process. The lengths of the BNNTs are estimated at a few micrometers based on observations of individual isolated nanotubes in the SEM images.

TEM images confirm that the fibrous materials observed in the reaction products have hollow tubular structures with multiple highly crystalline walls (Figure 3). The majority of the nanotubes have between 2 and 5 walls and diameters of less than 10 nm (Figure S12 shows the size distribution of the BNNTs produced). No nanotubes with diameters greater than 15 nm were observed throughout the samples. The average diameter is estimated as ~5 nm, and the most frequently observed diameter was 3 nm, suggesting a high selectivity of our process toward small-diameter BNNTs. The elemental composition of the nanotubes was assessed by electron energy loss spectroscopy (EELS) measurements. Figure 3E shows an EELS spectrum of a BNNT having a diameter of ~5 nm. The K-shell ionization edges of B (189 eV) and N (401 eV) are clearly identified in the spectrum, which confirms the presence of B and N in the tube

walls. Moreover, the fine structures of the B and N K-edges display sharply defined π^* and σ^* peaks on the left side and right side of the edges, respectively. This is characteristic of sp^2-hybridized B$-$N networks and confirms the existence of a h-BN-like phase in the tube wall. A carbon peak at 284 eV is also observable; however, the C K-edge is broad with a weak π^* signature, implying that carbon is present in an amorphous phase rather than a sp^2-hybridized phase. Figure 3F shows zero-loss energy-filtered images and elemental maps of the same nanotube. The elemental maps clearly reveal that B and N are uniformly distributed along the entire walls of the nanotube, while C is localized to areas of contamination on the outer surface of the tube. Since our feedstock and reaction gases are C-free, we believe that the C contamination originated from the adsorption of solvents employed during the TEM sample preparation.[29] If necessary, removal of such C impurities should be possible through thermal treatment (Figure S11) because the oxidation temperature of amorphous carbon (<500 °C) is lower than that of BNNT (>900 °C).[23]

The thermal stability of the as-grown BNNT materials has been investigated by thermogravimetric analysis (TGA). Both the fibril and cloth-like materials are stable up to 950 °C under air oxidation with slight increases in weight at higher temperatures (Figure S13). The onset of weight gain for both materials is approximately 650 °C and is attributed primarily to the oxidation of the amorphous B impurity present in the samples. The cloth-like sheet material showed a larger weight gain than the fibril material, suggesting that the fibril material contains a smaller amount of amorphous B impurity. Following the thermal extraction of B from

as-grown materials, no weight gain was observed during air oxidation up to 950 °C, suggesting effective removal of B and good thermal stability of the BNNTs produced in the plasma process (Figure S10).

Growth Mechanism and High Selectivity toward Small Diameters. Equilibrium calculations predict that the solid or gas phase of BN is stable only below 3500 K.[30] Considering the high temperatures in our process (over 5000 K), the h-BN powder injected is expected to be efficiently decomposed into its elementary species of B and N inside the plasma jet. This is in line with our experimental observation that brown or black flaky powders (*i.e.*, amorphous B) were the primary products under non-optimum conditions due to the recombination of N liberated during vaporization of h-BN into N_2. The nucleation and growth mechanism of BNNTs from those vapors was found to be consistent with what has been proposed for the laser synthesis process (Figure S3):[27] This root growth mechanism is supported by TEM images of our as-grown BNNT material, which clearly show BNNTs protruding from amorphous B particles encapsulated by h-BN shells (Figure S3).

Unlike other BNNT synthesis processes, the B vapors generated in our process undergo rapid cooling due to expansion of the plasma jet at the entrance of the reactor. Numerical simulations of our reaction conditions (Figure S2) indicate a cooling rate of $\sim 10^5$ K/s through the first 0.6 m of the reactor. This exceptionally high cooling rate provides a strong driving force for nucleation of small-diameter B droplets and limits their subsequent growth, which is crucial for the formation of small-diameter BNNTs exclusively. Due to this unique feature, small-diameter BNNTs are produced without the need for metal catalysts or additional condensers.

Catalytic Role of Hydrogen. Our main finding is that the presence of hydrogen gas in the reaction mixture is essential to the production of both high-purity and high-yield BNNTs by this induction thermal plasma method. According to the root growth mechanism discussed above (Figure S3), interactions between B droplets and N sources downstream are crucial for growth of BNNTs from the B droplets through the renitriding process. However, our numerical simulation results reveal that the residence time of B droplets in our reactor is as short as $\sim$100 ms, implying that the fast in-flight reaction between B droplets and N-containing species is the key for achieving high-yield production of BNNTs. In the absence of hydrogen, the main source of nitrogen for BNNT growth is relatively inert N_2 molecules, as N radicals freed from the dissociation of BN or N_2 gases will quickly recombine into N_2 at high temperatures (>5000 K) before the temperature reaches a suitable range for the formation B droplets and, subsequently, BNNT growth (>3000 K). The direct combination of B and N_2 into a h-BN phase (*i.e.*, $2B + N_2 \rightarrow 2BN$) is known to be extremely slow owing to the strong triple bond of nitrogen (dissociation energy = 945 kJ/mol).
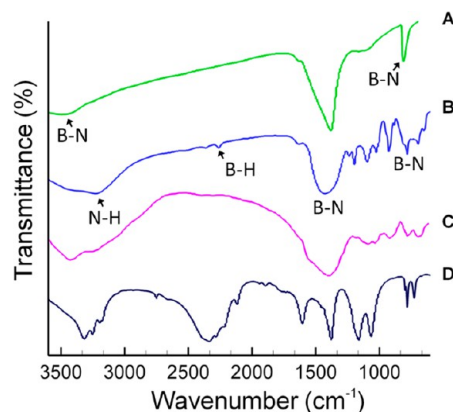

Figure 4. FT-IR analysis on the as-grown BNNT material and reaction byproduct extracted. FT-IR spectra of as-grown BNNT material (A), reaction byproduct extracted from the as-grown BNNT material (B), ammonia borane heated to 900 °C (C),[32] and ammonia borane (D). The FT-IR spectrum of the reaction byproduct (blue line) exhibits absorption peaks corresponding to N—H, B—H, and B—N bonds, which confirm the formation of B—N—H-containing species from a mixture of h-BN, N_2, and H_2 in the BNNT synthesis by an induction plasma.

The very low yield of BNNTs and the abundance of amorphous boron obtained in the absence of hydrogen in our early experiment is a strong illustration of the inefficiency of direct recombination of B and N_2 into a h-BN-like phase over such short time scale (Figure S4).

We found that the addition of hydrogen results in the production and stabilization of B—N—H-containing intermediate species which impede the recombination of N radicals generated by the vaporization into N_2 and provide faster and thermodynamically more efficient chemical pathways to the re-formation of a h-BN-like phase in B droplets during BNNT nucleation than the direct B—N_2 reaction (Figure S5). Infrared spectra of the as-grown BNNT material as well as reaction byproducts that were extracted from the as-produced material postproduction support this assertion (Figure 4; see Figures S6—S8 for additional details). The FT-IR spectrum of reaction byproducts extracted from the as-grown material (Figure 4B) clearly shows absorption peaks corresponding to N—H and B—H bonds appearing near 3200 and 2260 cm^{-1}, respectively, as well as the in-plane B—N stretching mode at 1390 cm^{-1}. In addition, the out-of-plane B—N—B bending mode at 780 cm^{-1} is observed, suggesting the presence of a B_3N_3 ring-like structure.[31—33] For comparison, the spectra of pristine and thermally treated ammonia borane (BH_3NH_3) are also shown since compounds such as this and borazine ($H_6B_3N_3$), or their polymers, are known to be effective precursors for the production of h-BN, particularly at elevated temperatures.[31—33] The spectrum of the reaction byproducts shows a strong similarity to thermally treated ammonia borane. We interpret this to indicate that the byproducts are a mixture of materials with similarities in structure to ammonia borane and its polymers and originate from reaction intermediates that
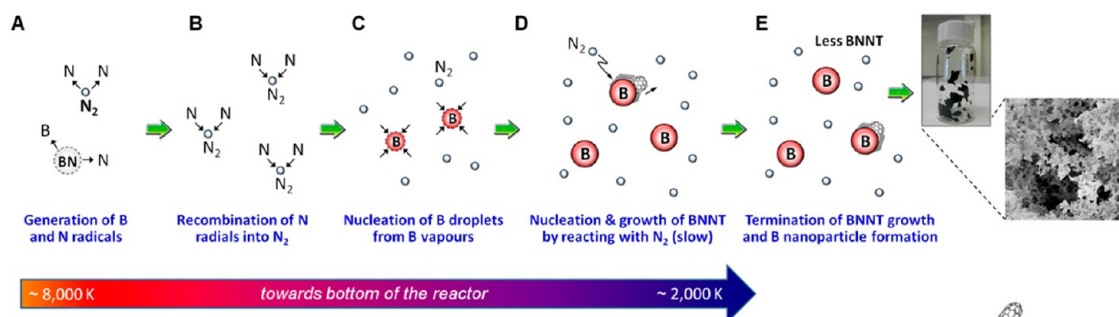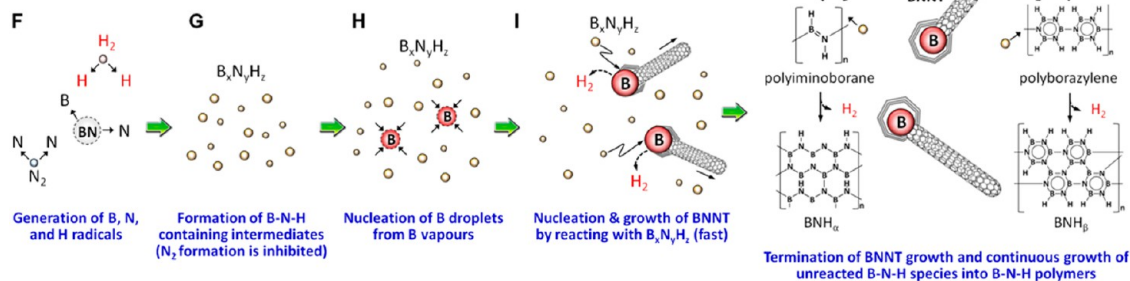
Growth mechanism without H₂:

A Generation of B and N radicals

B Recombination of N radials into N₂

C Nucleation of B droplets from B vapours

D Nucleation & growth of BNNT by reacting with N₂ (slow)

E Termination of BNNT growth and B nanoparticle formation

~ 8,000 K   *towards bottom of the reactor*   ~ 2,000 K

Growth mechanism with H₂:

F Generation of B, N, and H radicals

G Formation of B-N-H containing intermediates (N₂ formation is inhibited)

H Nucleation of B droplets from B vapours

I Nucleation & growth of BNNT by reacting with BₓNᵧH_z (fast)

J polyiminoborane   polyborazylene   BNHα   BNHβ

Termination of BNNT growth and continuous growth of unreacted B-N-H species into B-N-H polymers

Figure 5. Schematic representation of nucleation and growth mechanism of BNNT in an induction plasma process. Nucleation and growth mechanism of BNNTs in the absence of hydrogen (A−E) and in the presence of hydrogen (F−I). The key role played by hydrogen in the high-yield growth of BNNTs by an induction plasma process is the production and stabilization of B−N−H-containing intermediates, which impede the recombination of N radicals into N₂ and also provide faster and thermodynamically more efficient chemical pathways to the re-formation of a h-BN-like phase in B droplets.

are not fully consumed before the BNNT growth process is quenched. The spectrum of BNNT shows no evidence of N−H or B−H bonds and resembles very closely the spectrum of pure h-BN powder (see Figure S8). Gaseous byproducts absorbed into the as-grown BNNT material have also been investigated by TGA under desorption mode, and the FT-IR measurement of the evolved gas shows the presence of ammonia (NH₃; see Figure S9); ammonia is not used as a feedstock or reactant in this process, so its observation confirms that it is produced during the synthesis reaction. These observations confirm that B−N−H-containing intermediates were generated following plasma vaporization and were sufficiently stable to survive the conditions within the reactor.

The critical role of hydrogen and the selectivity of this plasma process toward the synthesis of small-diameter BNNTs are consistent with a reaction and growth mechanism that is summarized in Figure 5. In the initial stage of the process, H, B, and N radicals are generated from the vaporization of the feedstock mixture. The presence of H radicals largely inhibits the tendency for the liberated N to rapidly combine to produce N₂, instead forming N−H, B−H, and B−N−H intermediate species. The reaction stream then undergoes very rapid cooling, which favors the condensation of vaporized boron into nanometric droplets. This is crucial to the nucleation of small-diameter BNNTs exclusively. The rate of cooling then decreases as the reaction mixture approaches the liquid−solid phase transition temperature of the binary B−N

system (∼2300 K),[34] which promotes an uptake of nitrogen (supplied by the hydrogen-stabilized intermediate species) by the boron seed particles and an extended period of nucleation and growth of BNNTs. The exposure of the BNNTs to the high temperatures of this process throughout growth contributes to the high degree of crystallinity in the sidewall structure due to rapid annealing of defects. The growth of BNNTs is terminated either by a temperature drop below a critical value or by encapsulation of B droplets with h-BN shells, seen by TEM (Figure S3), and the B−N−H-containing intermediate species that do not participate directly in BNNT growth lead to the formation of borane-like and borazine-like byproducts, as observed by FT-IR (Figures 4, S6, and S7), as the reaction mixture continues to cool.

The generation of H and N radicals is a key differentiator between this plasma synthesis process and others reported in the literature. The high-enthalpy plasma can readily dissociate molecular gases like BN, N₂, and H₂ with high efficiency, which can subsequently contribute to the formation of reactive intermediates that are more favorable precursors to BNNT nucleation and growth. This likely explains the difference in the significance hydrogen plays in this process compared to lower temperature processes reported in the literature. It is also noted that, although essential for high-yield production of BNNT, hydrogen in this plasma process is not directly consumed during the nucleation and growth of the nanotubes. As such,
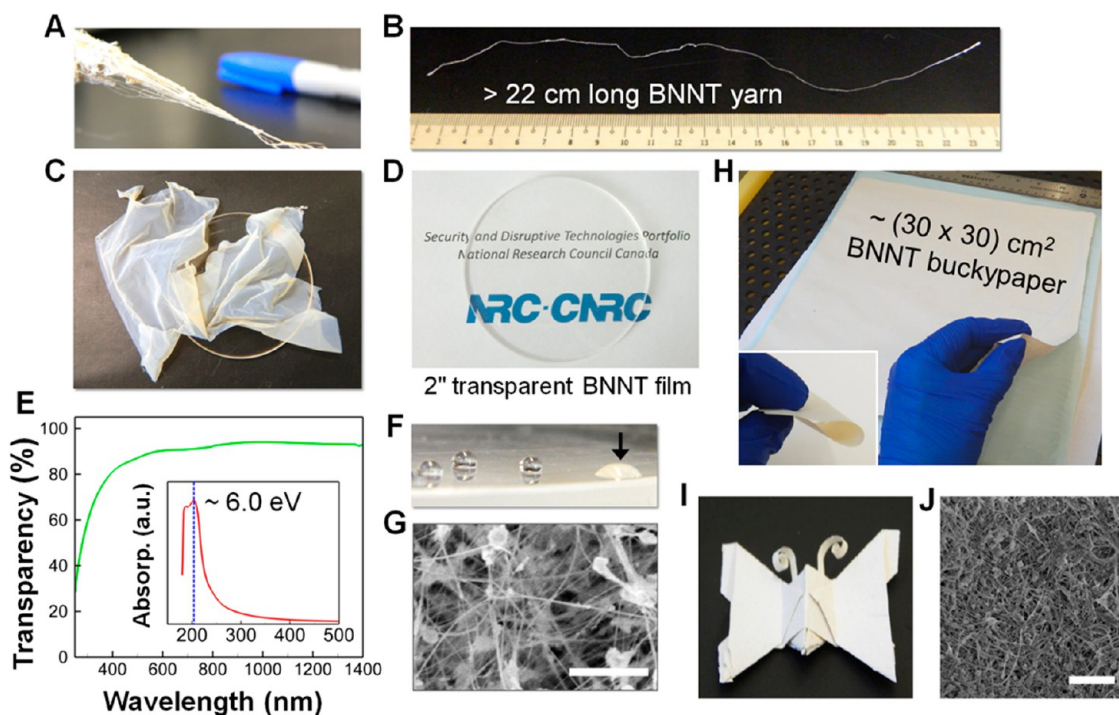
Figure 6. Large-scale, macroscopic assemblies of BNNTs. (A) BNNT fibrils drawn directly from the as-grown fibril material by hand-pulling. (B) BNNT yarn in excess of 22 cm in length spun from the fibrils *via* finger-twisting. (C) Free-standing BNNT thin film produced *in situ*. (D) Transparent BNNT thin film transferred to a 2 in. quartz disk. The BNNT film (thickness = ~0.2 μm) is almost invisible due to its high band gap (~6.0 eV). (E) Transmission and absorption characteristics of the BNNT thin film in the UV−vis range. Strong absorption at ~200 nm indicates the existence of a h-BN phase. (F) Hydrophobicity of the transparent thin film. The arrow indicates a spot without coverage of the BNNT thin film. (G) SEM image of the thin film. The scale bar is 0.5 μm. (H) Flexible BNNT buckypapers, up to 30 × 30 cm^2 in area, produced by vacuum filtration of liquid suspensions. (I) Material is foldable, as demonstrated with an origami butterfly folded from an 8 cm × 8 cm buckypaper. (J) SEM image of a BNNT buckypaper. The scale bar is 1.0 μm.

hydrogen is considered to play a catalytic role in the growth of BNNT in this process. Some of the hydrogen that stabilizes the B−N−H-containing intermediates is incorporated into the reaction byproducts, while much is eventually regenerated as hydrogen gas.

Macroscopic Assemblies of Boron Nitride Nanotubes. Material architectures such as yarns, buckypapers, sheets, and transparent thin films are highly advantageous for exploiting the properties of nanomaterials in a wide range of applications. To date, demonstrations of the assembly of BNNTs into larger architectures have been isolated to a 3 cm long finger-twisted yarn,[24] due primarily to the very limited availability of BNNTs. Here we show that our finding has immediate impacts on broad areas of science and technology by making the first demonstration of the fabrication of macroscopic assemblies of BNNT at large scales. The diversity in the macroscopic morphology of the BNNT product material from our process also lends to its easy adaption in many of these different application areas. The higher density and alignment within the fibril deposits enabled the drawing of long yarns in excess of 20 cm in length directly from the as-grown material that could be further densified by finger-twisting and solvent-spraying (Figure 6A,B and Figure S14). These crudely spun yarns are mechanically strong enough to support

weight (7.3 g, Figure S14) and to perform mechanical tests. Preliminary mechanical measurements present Young's modulus of around 0.5 GPa and tensile strength of around 10 MPa, respectively. The purity and yield of the as-grown fibril deposit is high enough that continuous spinning of BNNT yarns directly from the synthesis reactor is feasible and is currently being investigated.

The cloth-like deposits formed directly in the reactor are mainly collected as four large sheets (approximately 20 cm × 50 cm, a few millimeters thick) that are flexible and mechanically robust. Interestingly, this material is composed of multiple layers, where the number of layers and total thickness depend on the synthesis time, and thin diaphanous membranes can be easily peeled off as demonstrated in Figure 1D. Transparent thin films of BNNTs can be readily separated from the cloth-like deposits, as well as from some of the surfaces within the synthesis reactor, and represent the first demonstration of such architectures in the reported literature. These films are stretchable, highly electrostatic, and mechanically strong enough to stand without supports, as shown in Figure 6C. To assess the optical properties of the films, they were directly transferred to a quartz disk and adhered *via* a simple methanol spraying. The films are highly

transparent (Figure 6D). Figure 6E shows the absorption and transmittance properties of a film with ~0.2 μm thickness that had been baked at 425 °C in air overnight in order to remove the trace amorphous boron. Good transmittance is obtained over a broad wavelength range, which is very promising for transparent electronic devices or composite applications. The absorption peak observed around 200 nm (inset of Figure 6E) is consistent with the presence of a h-BN-like phase in the film and corresponds to a band gap of about 6.0 eV. The shoulder peak below 190 nm may originate from the quartz disk. The transparent films also exhibit hydrophobicity as shown in Figure 6F. Electron microscopy reveals that the films are composed of a mat of entangled BNNTs (Figure 6G).

Macroscopic architectures also have been produced *via* liquid processing of this BNNT material, as was the case for buckypapers (Figure 6H−J) produced by a vacuum filtration method (Figure S14) analogous to approaches employed for CNT buckypaper.[35] Flexible BNNT buckypapers from ~15 to 150 μm in thickness and up to 30 cm × 30 cm in area have been produced. The density of these papers was 0.4−0.5 g/cm^3, and they can be folded without cracking (Figure 6I). Early mechanical tests indicated that the Young's modulus and ultimate tensile strength were typically ~0.3 GPa and 1.5 MPa, respectively, with strengths up to 3 MPa observed.

The very low density, cotton-like BNNT material covers the entire interior surface of the filtration chamber of the reactor (Figure 1E). Due to its unique morphology of very loosely entangled BNNTs, this material demonstrates high hydrophobicity as shown in the inset of Figure 2D. This material also exhibits a strong photoacoustic response when exposed to a camera flash (video S1). Similarly to what has been reported for low-density SWCNT materials exposed to intense light pulses,[36] these BNNT deposits emit an audible noise following exposure to a camera flash. Unlike SWCNTs, however, the BNNTs do not undergo combustion due to their higher thermal stability and the absence of metal catalysts.

CONCLUSIONS

By using an induction thermal plasma, large amounts of small-diameter BNNTs are successfully produced at an unprecedentedly high rate approaching 20 g/h, without the need for metal catalysts. The BNNTs have few walls and are highly crystalline with an excellent cylindrical geometry and average diameter of ~5 nm, implying a high selectivity of the process toward highly crystalline small-diameter BNNTs. The numerical simulation and TEM results suggested that exceptionally rapid cooling of the reaction stream (~10^5 K/s) favors the condensation of B into small-sized droplets is responsible for the nucleation of small-diameter BNNTs exclusively. It was also found that hydrogen plays a crucial, catalytic role in the high-rate and high-yield growth of BNNTs by inhibiting the formation of N_2 from N radicals and promoting the creation of B−N−H intermediate species, which provide faster chemical pathways to the re-formation of a h-BN-like phase. The yields demonstrated by this plasma synthesis process mean that kilogram quantities of high-purity and highly crystalline BNNTs are now accessible for the first time. The process also has good potential for cost-effective scalability as the core technology is mature, with high-power plasma torches up to ~MW levels available,[37] and the gases and feedstock are all inexpensive materials. These results, coupled with the fact that gas-flow-driven deposits in the reactor naturally form macroscopic architectures that are easily adaptable to producing large-scale fibers, fabrics, thin films, and buckypapers, represent a seminal milestone toward the exploitation of BNNTs in real-world applications.

METHODS

Induction Plasma Processing System. The induction plasma system developed in this work consists of four major parts; an induction plasma torch, a reaction chamber, a filtration chamber, and feedstock delivery (Figure S1). The induction plasma torch is a commercial TEKNA PS-50 torch (Tekna Plasma Systems, Inc.) composed of a five-turn coil and a ceramic tube with an internal diameter of 50 mm. The torch is driven by a RF power supply (Lepel Co.) operated at an oscillator frequency of ~3.6 MHz, the maximum plate power being 60 kW. The reaction chamber includes a 1 m long graphite liner surrounded by thermal insulating wool, in order to extend the high-temperature zone needed for an effective growth of BNNTs. The feedstock is continuously fed by a powder feeder (KT20 twin-screw microfeeder, K-Tron, Inc.) and delivered to an injection probe located on the top of the plasma torch by Ar carrier gas. The main reaction products are collected from four porous metal filter units (surface area = 20 × 50 cm, 2.8 μm pore size) inside a filtration chamber connected to the end of the reaction chamber (not shown in Figure S1).

BNNT Synthesis Protocol. The synthesis experiments were performed at a fixed plate power of 50 kW (30−35 kW of net plasma power) and a base pressure of 93 kPa. Initially, the reactor was purged and filled with Ar gas. Afterward, two different gas streams were introduced into the plasma torch; pure Ar gas (30 slpm) was injected into the central region of the torch for stable plasma generation, and a ternary gas mixture of Ar (45 slpm), N_2 (55 slpm), and H_2 (20 slpm) was introduced as a high-velocity laminar flow around the plasma, offering further plasma stabilization and chemical reactions downstream of the plasma plume. The synthesis experiments were preceded by a 1 h reactor preheating cycle to heat the upper graphite liner to approximately 1200 °C. At this point, feedstock delivery was started and synthesis lasted for 3−4 h. Pure hexagonal boron nitride (h-BN) powder (99.5%, avg. 70 nm, MK-hBN-N70, MK Impex Corp.) was used as a starting material and was prepared by drying at 100 °C for 24 h. No catalyst was employed. The h-BN powder was carried from the powder feeder to the plasma by using 3 slpm of Ar carrier gas. In a typical synthesis experiment, the feed rate of the h-BN powder was 0.5−1.0 g/min. The main reaction product was collected in the filtration chamber.

Fabrication of Large-Scale BNNT Buckypaper. Following removal of amorphous boron as described in the Supporting Information,

BNNTs were dispersed in liquid (water or methanol) using a combination of stirring, and horn and bath sonication to produce a fluffy dispersion that is stable for short periods of time. The dispersion was then vacuum-filtered using either standard laboratory filtration equipment to produce ~3.5 cm diameter circular buckypapers or a home-built vacuum table with custom size, rectangular funnels (up to 30 cm × 30 cm) to produce larger buckypapers (Figure S14). In all cases, the dispersion was filtered through 20 μm pore size polycarbonate membranes, which were available as both 47 mm diameter circles (Sterlitech PCT20047100) and 30 cm × 300 cm rolls (Sterlitech PCT2003001). A vacuum gauge and soap solution were used to check for leaks in the home-built setup, as good suction is required to get a condensed paper. The as-filtered buckypapers were sandwiched between sheets of parchment paper and compressed. After drying (or partial drying) at room temperature, the buckypapers were easily peeled from the membrane. The room-temperature-dried buckypapers were further dried at 100 °C for 2 h.

Material Characterization. The material properties of the BNNT samples produced were analyzed by SEM (Hitachi, S4700), TEM (FEI Titan cubed 80−300), TGA (Netzsch TG 209 F1 Iris), FT-IR (Nicolet 6700 FT-IR), and UV−vis−NIR absorption spectroscopy (Cary 5000, Varian). For SEM, it was necessary to coat the BNNT samples with a thin layer of gold using a sputter coater (Edwards S150A) prior to imaging to prevent electron charging. Voltage was adjusted to obtain a current of 40 mA with a gold coating deposition time of 5 s. Each sample was imaged with a 2 kV, 5 μA probe current at a working distance of 4 mm. The TEM analysis was performed at the Canadian Centre for Electron Microscopy at McMaster University. High-resolution TEM images and EELS data were acquired at 80 kV. The microscope was equipped with 2 CEOS correctors. TGA data were obtained by heating a ~10 mg sample under an air atmosphere to 950 °C at a rate of 10 °C/min. Absorption spectroscopy was attained by attaching the quartz disk (possessing the BNNT film) to the sample port while using air as a reference. In the FT-IR analysis, samples were prepared by grinding with KBr powder and pressing into disc pellets. Tensile tests on buckypaper strips (5 or 10 mm in width) were performed using a 10 lb load cell on a Fullam substage test frame at a displacement rate of 0.5 mm/min. The displacement of the grips was used to determine strain.

Numerical Simulation. The plasma generation was described by employing the magneto-hydrodynamic equations for conservations of mass, momentum, and energy, along with the $K-\varepsilon$ turbulence model. The thermodynamic and transport properties of the plasma gases (e.g., density, specific heat at constant pressure, viscosity, thermal conductivity, electrical conductivity, and radiation losses) were obtained from the tabulated data, which were calculated with the assumption of the local thermodynamic equilibrium.[38] The detailed method for the numerical simulation can be found elsewhere.[39] The injection of feedstock and chemical reactions which led to the nucleation and growth of BNNTs were not considered at this moment.

Conflict of Interest: The authors declare no competing financial interest.

Supporting Information Available: Induction plasma process; nucleation and growth mechanism of BNNTs; role of hydrogen; BNNT synthesis from B powder; purification of BNNTs; conversion efficiency of h-BN into BNNTs; diameter and wall number distribution of BNNTs; thermal stability of BNNTs; fabrication of macroscopic assemblies of BNNTs. This material is available free of charge via the Internet at http://pubs.acs.org.

REFERENCES AND NOTES

1. Arenal, R.; Wang, M.-S.; Xu, Z.; Loiseau, A.; Golberg, D. Young Modulus, Mechanical and Electrical Properties of Isolated Individual and Bundled Single-Walled Boron Nitride Nanotubes. *Nanotechnology* **2011**, *22*, 265704.
2. Blase, X.; Rubio, A.; Louie, G.; Cohen, M. L. Stability and Band Gap Constancy of Boron Nitride Nanotubes. *Europhys. Lett.* **1994**, *28*, 335–340.
3. Arenal, R.; Blase, X.; Loiseau, A. Boron-Nitride and Boron-Carbonitride Nanotubes: Synthesis, Characterization and Theory. *Adv. Phys.* **2010**, *59*, 101–179.
4. Chen, Y.; Zou, J.; Campbell, S. J.; Le Caer, G. Boron Nitride Nanotubes: Pronounced Resistance to Oxidation. *Appl. Phys. Lett.* **2004**, *84*, 2430–2432.
5. Chopra, N. G.; Luyken, R. J.; Cherrey, K.; Crespi1, V. H.; Cohen, M. L.; Louie, S. G.; Zettl, A. Boron Nitride Nanotubes. *Science* **1995**, *269*, 966–967.
6. Golberg, D.; Bando, Y.; Tang, C. C.; Zhi, C. Y. Boron Nitride Nanotubes. *Adv. Mater.* **2007**, *19*, 2413–2432.
7. Rao, C. N. R.; Govindaraj, A. Synthesis of Inorganic Nanotubes. *Adv. Mater.* **2009**, *21*, 4208–4233.
8. Zhi, C. Y.; Bando, Y.; Tang, C. C.; Golberg, D. Boron Nitride Nanotubes. *Mater. Sci. Eng. Res.* **2010**, *70*, 92–111.
9. Golberg, D.; Bando, Y.; Huang, Y.; Terao, T.; Mitome, M.; Tang, C.; Zhi, C. Boron Nitride Nanotubes and Nanosheets. *ACS Nano* **2010**, *4*, 2979–2993.
10. Cumings, J.; Zettl, A. Mass-Production of Boron Nitride Double-Wall Nanotubes and Nanococoons. *Chem. Phys. Lett.* **2000**, *316*, 211–216.
11. Laude, T.; Matsui, Y.; Marraud, A.; Jouffrey, B. Long Ropes of Boron Nitride Nanotubes Grown by a Continuous Laser Heating. *Appl. Phys. Lett.* **2000**, *76*, 3239–3241.
12. Tang, C.; Bando, Y.; Sato, T.; Kurashima, K. A Novel Precursor for Synthesis of Pure Boron Nitride Nanotubes. *Chem. Commun.* **2002**, *76*, 1290–1291.
13. Zhi, C. Y.; Bando, Y.; Tang, C. C.; Golberg, D. Effective Precursor for High Yield Synthesis of Pure BN Nanotubes. *Solid State Commun.* **2005**, *135*, 67–70.
14. Lee, C. H.; Wang, J. S.; Kayatsha, V. K.; Huang, J. Y.; Yap, Y. K. Effective Growth of Boron Nitride Nanotubes by Thermal Chemical Vapor Deposition. *Nanotechnology* **2008**, *19*, 455605.
15. Chen, Y.; Fitz Gerald, J.; Williams, J. S.; Bulcock, S. Synthesis of Boron Nitride Nanotubes at Low Temperatures Using Reactive Ball Milling. *Chem. Phys. Lett.* **1999**, *299*, 260–264.
16. Chen, Y.; Conway, M.; Williams, J. S.; Zou, J. Large-Quantity Production of High-Yield Boron Nitride Nanotubes. *J. Mater. Res.* **2002**, *8*, 1896–1899.
17. Sen, R.; Satishkumar, B. C.; Govindaraj, A.; Harikumar, K. R.; Raina, G.; Zhang, J.-P.; Cheetham, A. K.; Rao, C. N. R. B−C−N, C−N and B−N Nanotubes Produced by the Pyrolysis of Precursor Molecules over Co Catalysts. *Chem. Phys. Lett.* **1998**, *287*, 671–676.
18. Lee, C. M.; Choi, S. I; Choi, S. S.; Hong, S. H. Synthesis of Boron Nitride Nanotubes by Arc-Jet Plasma. *Curr. Appl. Phys.* **2006**, *6*, 166–170.
19. Zhi, C.; Bando, Y.; Tang, C.; Honda, S.; Kuwahara, H.; Golberg, D. Boron Nitride Nanotubes/Polystyrene Composites. *J. Mater. Res.* **2006**, *21*, 2794–2800.
20. Loiseau, A.; Willaime, F.; Demoncy, N.; Hug, G.; Pascard, H. Boron Nitride Nanotubes with Reduced Numbers of Layers Synthesized by Arc Discharge. *Phys. Rev. Lett.* **1996**, *76*, 4737–4740.
21. Golberg, D.; Bando, Y.; Eremets, M.; Takemura, K.; Kurashima, K.; Yusa, H. Nanotubes in Boron Nitride Laser Heated at High Pressure. *Appl. Phys. Lett.* **1996**, *69*, 2045–2047.
22. Yu, J.; Chen, Y.; Wuhrer, R.; Liu, Z.; Ringer, S. P. In Situ Formation of BN Nanotubes during Nitriding Reactions. *Chem. Mater.* **2005**, *17*, 5172–5176.
23. Kim, M. J.; Chatterjee, S.; Kim, S. M.; Stach, E. A.; Bradley, M. G.; Pender, M. J.; Sneddon, L. G.; Maruyama, B. Double-Walled Boron Nitride Nanotubes Grown by Floating Catalyst Chemical Vapor Deposition. *Nano Lett.* **2008**, *8*, 3298–3302.
24. Smith, M. W.; Jordan, K. C.; Park, C.; Kim, J.-W.; Lillehei, P. T.; Crooks, R.; Harrison, J. S. Very Long Single- and Few-Walled

Boron Nitride Nanotubes *via* the Pressurized Vapor/Condenser Method. *Nanotechnology* **2009**, *20*, 505604.

25. Huang, Y.; Lin, J.; Tang, C.; Bando, Y.; Zhi, C.; Zhai, T.; Dierre, B.; Sekiguchi, T.; Golberg, D. Bulk Synthesis, Growth Mechanism and Properties of Highly Pure Ultrafine Boron Nitride Nanotubes with Diameters of Sub-10 nm. *Nanotechnology* **2011**, *22*, 145602.

26. Kim, K. S.; Cota-Sanchez, G.; Kingston, C. T.; Imris, M.; Simard, B.; Soucy, G. Large-Scale Production of Single-Walled Carbon Nanotubes by Induction Thermal Plasma. *J. Phys. D: Appl. Phys.* **2007**, *40*, 2375–2387.

27. Arenal, R.; Stephan, O.; Cochon, J. L.; Loiseau, A. Root-Growth Mechanism for Single-Walled Boron Nitride Nanotubes in Laser Vaporization Technique. *J. Am. Chem. Soc.* **2007**, *129*, 16183–16189.

28. Yu, J.; Li, B. C. P.; Zou, J.; Chen, Y. Influence of Nitriding Gases on the Growth of Boron Nitride Nanotubes. *J. Mater. Sci.* **2007**, *42*, 4025–4030.

29. Kim, J.- W.; Núñez, J. C.; Siochi, E. J.; Wise, K. E.; Lin, Y.; Connell, J. W.; Smith, M. W. *In Situ* Mechanical Property Measurements of Amorphous Carbon−Boron Nitride Nanotube Nanostructures. *Nanotechnology* **2012**, *23*, 035701.

30. Watanabe, T.; Sataka, R.; Yamamoto, K. Effect of Bias Application on c-BN Synthesis by Induction Thermal Plasmas under Atmospheric Pressure. *Thin Solid Films* **2008**, *516*, 4462–4467.

31. Frueh, S.; Kellett, R.; Mallery, C.; Molter, T.; Willis, W. S.; King'ondu, C.; Suib, S. L. Pyrolytic Decomposition of Ammonia Borane to Boron Nitride. *Inorg. Chem.* **2011**, *50*, 783–792.

32. Fazen, P. J.; Remsen, E. E.; Beck, J. S.; Carroll, P. J.; McGhie, A. R.; Sneddon, L. G. Synthesis, Properties, and Ceramic Conversion Reactions of Polyborazylene—A High-Yield Polymeric Precursor to Boron-Nitride. *Mater. Chem.* **1995**, *101*, 1942–1956.

33. Wang, X.; Zhi, C.; Li, L.; Zeng, H.; Li, C.; Mitome, M.; Golberg, D.; Bando, Y. "Chemical Blowing" of Thin-Walled Bubbles: High-Throughput Fabrication of Large-Area, Few-Layered BN and C$_x$-BN Nanosheets. *Adv. Mater.* **2011**, *23*, 4072–4076.

34. Okamoto, H. B-N (Boron-Nitrogen). *J. Phase Equilib.* **2000**, *21*, 208–208.

35. Ashrafi, B.; Guan, J.; Mirjalili, V.; Hubert, P.; Simard, B.; Johnston, A. Correlation between Young's Modulus and Impregnation Quality of Epoxy-Impregnated SWCNT Buckypaper. *Composites A* **2010**, *41*, 184–191.

36. Ajayan, P. M.; Terrones, M.; de la Guardia, A.; Huc, V.; Grobert, N.; Wei, B. Q.; Lezec, H.; Ramanath, G. Nanotubes in a Flash−Ignition and Reconstruction. *Science* **2002**, *296*, 705.

37. Boulos, M. I. The Inductively Coupled R.F. (Radio Frequency) Plasma. *Pure Appl. Chem.* **1985**, *57*, 1321–1352.

38. Boulos, M. I.; Fauchais, P.; Pfender, E. *Thermal Plasmas, Fundamentals and Applications*; Plenum: New York, 1994.

39. Kim, K. S.; Moradian, A.; Mostaghimi, J.; Yasaman, A.; Shahverdi, A.; Simard, B.; Soucy, G. Synthesis of Single-Walled Carbon Nanotubes by Induction Thermal Plasma. *Nano Res.* **2009**, *2*, 800–817.